Analysis and Modeling of a Gain-Boosted N-Path Switched-Capacitor Bandpass Filter

Zhicheng Lin, *Graduate Student Member, IEEE*, Pui-In Mak, *Senior Member, IEEE*, and Rui P. Martins, *Fellow, IEEE*

***Abstract*—It has been studied that, an N-path switched-capacitor (SC) branch driven by an N-phase non-overlapped local oscillator (LO), is equivalent to a tunable parallel-RLC tank suitable for radio-frequency (RF) filtering. This paper proposes a *gain-boosted N-path SC bandpass filter (GB-BPF)* with a number of sought features. It is based on a transconductance amplifier (G_m) with an N-path SC branch as its feedback network, offering: 1) double RF filtering at the input and output of the G_m in one step; 2) customized passband gain and bandwidth with input-impedance match; and 3) reduced physical capacitance thanks to the loop gain offered by G_m. All have been examined using a RLC model of the SC branch before applying the linear periodically time-variant (LPTV) analysis to derive the R, L, and C expressions and analytically study the harmonic selectivity, harmonic folding, and noise. The latter reveals that: 1) the noise due to the switches is notched at the output, allowing smaller switches to save the LO power and 2) the noises due to the source resistance and G_m are narrowband at the output, reducing the folded noise during harmonic mixing. To study the influence of circuit non-idealities, an intuitive equivalent circuit model is also proposed and verified. The design example is a four-path 0.5–2-GHz GB-BPF simulated with the 65-nm CMOS. It exhibits >11 dB gain, <2.3 dB NF, and +21-dBm out-of-band IIP3 at 150-MHz offset, while consuming just 7 mW of power.**

***Index Terms*—Bandpass filter, bandwidth, CMOS, feedback network, gain boosted, harmonic mixing, input-impedance match, linear periodically time-variant (LPTV), local oscillator (LO), N-path, passive mixer, receiver, radio-frequency (RF) filtering, switched-capacitor (SC), switches, transconductance amplifier.**

I. Introduction

THE demand of highly integrated multiband transceivers has driven the development of blocker-tolerant software-defined radios that can avoid the cost (and loss) of the baluns and SAW filters [1]–[3]. The passive-mixer-first receivers [1], [2] achieve a high out-of-band (OB) linearity (IIP3 $= +25$ dBm) by eliminating the forefront low-noise amplifier (LNA). However, in the absence of radio-frequency (RF) gain, a considerable amount of power is entailed for the local oscillator (LO) to drive up the mixers that must be essentially large (i.e., small on-resistance, R_{sw}) for an affordable noise figure (NF < 5 dB). The noise-cancelling receiver in [3] breaks such a NF-linearity tradeoff, by noise-cancelling the main path via a high-gain auxiliary path, resulting in better NF (1.9 dB). However, due to the wideband nature of all RF nodes, the passive mixers of the auxiliary path should still be large enough for a small R_{sw} (10 Ω) such that the linearity is upheld (IIP3 $= +13.5$ dBm). Indeed, it would be more effective to perform filtering at the antenna port.

An N-path switched-capacitor (SC) branch applied at the antenna port [4], [5] corresponds to direct filtering that enhances OB linearity, although the sharpness and ultimate rejection are limited by the capacitor size and non-zero R_{sw} that are tight tradeoffs with the area and LO power, respectively. Repeatedly adopting such filters at different RF nodes can raise the filtering order, but at the expense of power and area [5], [6].

Active-feedback frequency translation loop [7] is another technique to enhance the area efficiency (0.06 mm^2), narrowing RF bandwidth via signal cancellation, instead of increasing any RC time-constant. Still, the add-on circuitry (amplifiers and mixers) penalizes the power (62 mW) and NF (>7 dB). In [8], at the expense of more LO power and noise, the output voltages can be extracted from the capacitors via another set of switches, avoiding the effects of R_{sw} on the ultimate rejection, but the problem of area remains unsolved.

Recently, an ultra-low-power multiband ZigBee receiver [9] was demonstrated, which features a novel gain-boosted N-path passive mixer to optimize the NF and OB linearity with power. The underlying principle is generalized here for the first time, leading to a *gain-boosted N-path SC bandpass filter (GB-BPF)* with a number of attractive features: 1) tunability of center frequency, passband gain and bandwidth without affecting the input-impedance matching; 2) lower LO power as the pitfall of big R_{sw} can be leveraged by other design freedoms; and 3) much smaller capacitors for a given bandwidth thanks to the gain-boosting effects.

This paper is organized as follows: Section II introduces the proposed GB-BPF and describes its features via an ideal RLC model first. Linear periodically time-variant (LPTV) analysis is then followed to derive and examine the models of those R, L and C. The analysis of harmonic selectivity, harmonic folding and noise are detailed in Section III, where an equivalent circuit model for studying the influence of non-idealities is included. In Section IV, a simulation design example is given. Finally, the conclusions are drawn in Section V.

II. GB-BPF Using an Ideal RLC Model

The proposed GB-BPF is depicted in Fig. 1(a). It features a transconductance amplifier (G_m) in the forward path, and an N-path SC branch driven by an N-phase non-overlapped LO in the feedback path. When one of the switches is ON, an in-phase RF voltage V_{RF} will appear on the top plate of capacitor C_i, and induces an amplified anti-phase voltage into its bottom plate.

Manuscript received January 04, 2014; revised February 26, 2014; accepted March 13, 2014. Date of publication April 07, 2014; date of current version August 26, 2014. This work was supported in part by the University of Macau under Grant MYRG114-FST13-MPI and by the Macao Science and Technology Development Fund-FDCT. This paper was recommended by Associate Editor N. Krishnapura.

Z. Lin and P.-I. Mak are with the State-Key Laboratory of Analog and Mixed-Signal VLSI and FST-ECE, University of Macau, Macao, China (e-mail: yb07411@umac.mo; pimak@umac.mo).

R. P. Martins is with the State-Key Laboratory of Analog and Mixed-Signal VLSI and FST-ECE, University of Macau, Macao, China and also with the Instituto Superior Técnico, University of Lisbon, Portugal (e-mail: rmartins@umac.mo).

Color versions of one or more of the figures in this paper are available online at http://ieeexplore.ieee.org.

Digital Object Identifier 10.1109/TCSI.2014.2312476

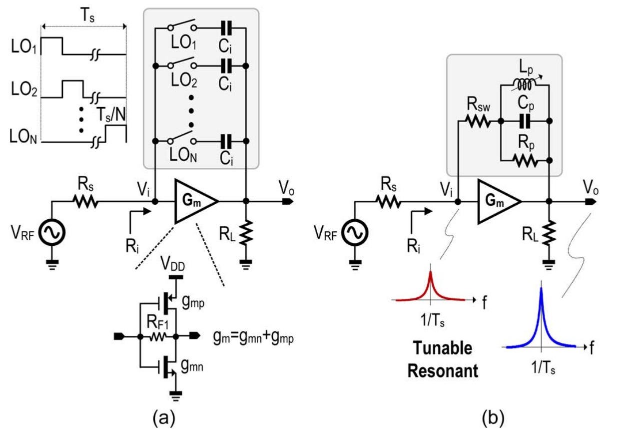

Fig. 1. (a) Proposed gain-boosted N-path SC bandpass filter (GB-BPF) and (b) its equivalent RLC circuit with the LC resonant tunable by the LO. R_{sw} is the mixer switch's on-resistance.

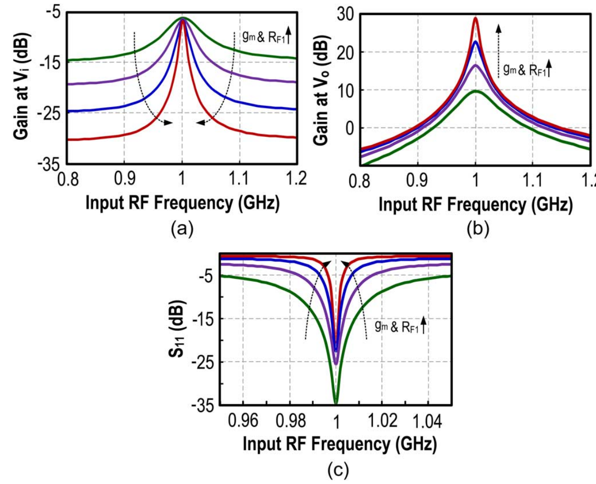

Fig. 2. Simulated (a) gain at V_i, (b) gain at V_o and (c) S_{11}, showing how g_m and R_{F1} tune the in-band gain and bandwidth while keeping the in-band S_{11} well below −20 dB.

When the switch is OFF, the amplified version of V_{RF} will be stored in C_i. There are three observations: 1) similar to the well-known capacitor-multiplying technique (i.e., Miller effect) in amplifiers, the effective capacitance of C_i at the input node V_i will be boosted by the loop gain created by G_m, while it is still C_i at the output node V_o. This feature, to be described later, reduces the required C_i when comparing it with the traditional passive N-path filter. 2) For the in-band signal, the voltages sampled at all C_i are in-phase summed at V_i and V_o after a complete LO switching period (T_s), while the OB blockers are cancelled to each other, resulting in double filtering at two RF nodes in one step. 3) As the switches are located in the feedback path, their effects to the OB rejection should be reduced when comparing it with the passive N-path filter.

For simplicity, G_m is assumed as an inverter amplifier with an effective transconductance of g_m. It is self-biased by the resistor R_{F1} and has a finite output resistance explicitly modeled as R_L. The parasitic effects will be discussed in Section III-C. With both passband gain and resistive input impedance, the GB-BPF can be directly connected to the antenna port for matching with the source impedance R_S. Around the switching frequency (ω_s), the N-path SC branch is modeled as an $R_p - L_p - C_p$ parallel network [10] in series with R_{sw}, where L_p is a function of ω_s and will resonate with C_p at ω_s [Fig. 1(b)]. The expressions of R_p, L_p and C_p will be derived in Section II-C. Here, the filtering behavior and −3-dB bandwidth at V_i and V_o will be analyzed.

A. RF Filtering at V_i and V_o

With V_{RF} centered at frequency $f_{RF} = f_s = \omega_s/2\pi$, L_P and C_p are resonated out, yielding an input resistance $R_i|_{@f_s}$ that can be sized to match R_S for the in-band signal

$$R_i|_{@f_s} = \frac{(R_p + R_{sw})//R_{F1} + R_L}{1 + g_m R_L} = R_S. \tag{1}$$

For the OB blockers located at $f_{RF} = f_s \pm \Delta f_s$, either L_p or C_p will become a short circuit when Δf_s is large enough

$$\begin{aligned} R_i|_{@f_s \pm \Delta f_s} &= \frac{(R_{sw}//R_{F1}) + R_L}{1 + g_m R_L} \\ &\approx \frac{R_{sw} + R_L}{1 + g_m R_L} \approx \frac{R_{sw}}{g_m R_L} + \frac{1}{g_m} \end{aligned} \tag{2}$$

where $R_{F1} \gg R_{sw}$ and $g_m R_L \gg 1$ are applied and reasonable to simplify (2). To achieve stronger rejection of OB blockers at V_i, a small $R_i|_{@f_s \pm \Delta f_s}$ is expected. Unlike the traditional passive N-path filter where the OB rejection is limited by R_{sw} [10], [15], this work can leverage it with three degrees of freedom: g_m, R_L and R_{sw}. As a GB-BPF at the forefront of a receiver, a large g_m is important to lower the NF of itself and its subsequent circuits. As an example, with $g_m = 100$ mS, the product of $g_m R_L$ can reach 8 V/V with $R_L = 80\ \Omega$. Thus, if $R_{sw} = 20\ \Omega$ is assumed, we obtain $R_i|_{@f_s \pm \Delta f_s} \approx 12.5\ \Omega$, which is only 62.5% of R_{sw}. If g_m is doubled (i.e., more power) while maintaining the same $g_m R_L$, $R_i|_{@f_s \pm \Delta f_s}$ is reduced to 7.5 Ω. Another way to trade the OB rejection with power is to adopt a multistage amplifier as G_m, which can potentially decouple the limited $g_m R_L$-product of a single-stage amplifier in nanoscale CMOS.

OB filtering not only happens at V_i, but also V_o. Hence, with one set of switches, double filtering is achieved in this work, leading to higher power and area efficiency than the traditional cascade design (i.e., two SC branches separately applied for V_i and V_o) as described in [5]. Likewise, the gain at V_o at the resonance can be found as

$$A_{vo}|_{@f_s} = \frac{V_o}{V_{RF}} = \frac{R_L(1 - g_m R_T)}{2R_S(1 + g_m R_L)} \approx \frac{R_L(1 - g_m R_T)}{2R_S g_m R_L} \tag{3}$$

where $R_T = R_{F1}//(R_p + R_{sw})$ and $g_m R_L \gg 1$ are applied In terms of stability, (3) should be negative or zero, i.e., $g_m R_T \leq 1$. Similarly, the gain at V_o at $f_s \pm \Delta f_s$ is derived when L_p or C_p is considered as a short circuit

$$\left.\frac{V_o}{V_{RF}}\right|_{@f_s \pm \Delta f_s} = \frac{1 - g_m R_{sw}}{1 + g_m R_S + \frac{R_S}{R_L} + \frac{R_{sw}}{R_L}}. \tag{4}$$

Interestingly, if $g_m R_{sw} = 1$, the OB filtering is infinite. This is possible because the feedback network is frequency selective, implying that the in-band signal and OB blockers can see different feedback factors. This fact differentiates this circuit from the traditional resistive-feedback wideband LNAs such as [11] that cannot help to reject the OB blockers.

To exemplify, the circuit of Fig. 1(a) is simulated for $N = 4$, using PSS and PAC analyses in SpectreRF. The parameters are: $R_{sw} = 20\ \Omega$, $R_L = 80\ \Omega$, $R_S = 50\ \Omega$, $C_i = 5$ pF and $f_s = 1$ GHz. As expected, higher selectivity at V_i [Fig. 2(a)] and V_o [Fig. 2(b)] can be observed when g_m (100 to 800 mS) and R_{F1} (500 to 8 kΩ) are concurrently raised, while preserving

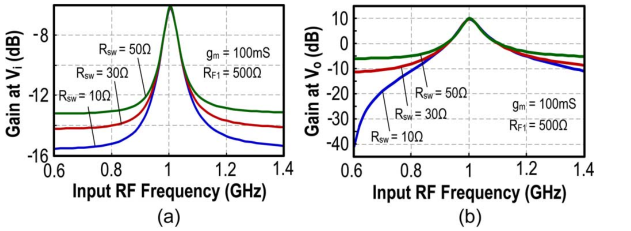

Fig. 3. Simulated (a) gain at V_i, (b) gain at V_o under $R_{sw} = 10$, 30 and 50 Ω.

the in-band $S_{11} < -20$ dB. [Fig. 2(c)]. Alternatively, when R_{sw} goes up from 10 to 50 Ω, with other parameters unchanged, it can be observed that the influence of R_{sw} to the OB rejection is relaxed at both V_i [Fig. 3(a)] and V_o [Fig. 3(b)], being well-consistent with (2) and (4). When $R_{sw} = 10\ \Omega$, a much stronger OB rejection is due to $g_m R_{sw}$ in (4).

B. −3-dB Bandwidth at V_i and V_o

At frequency $f_{RF} = f_s$, we can write $V_i/V_{RF}|_{@f_s} = 1/2$ when $R_i = R_s$. The −3-dB bandwidth is calculated by considering that the $L_p C_p$ tank only helps shifting the centre frequency of the circuit from DC to f_s, keeping the same bandwidth as it is without L_p. If R_{sw} is neglected and the Miller approximation is applied, the −3-dB passband bandwidth $(2\Delta f_{i3\text{ dB}})$ at V_i can be derived

$$2\Delta f_{i3\text{ dB}} = \frac{1}{\pi R_s C_i}; \quad C_i \approx (1 + A_{vi}) C_p \tag{5}$$

where

$$A_{vi} = \frac{V_o}{V_i} = \frac{R_L(1 - g_m R_T)}{R_S(1 + g_m R_L)}.$$

Obviously, C_p is boosted by a gain factor A_{vi}, which should be 15 to 20 dB in practice. Thus, a large A_{vi} can be used to improve the area efficiency, consistent with the desire of higher selectivity OB filtering, as shown in Fig. 2(a) and (b). Passive N-path filters [10] do not exhibit this advantageous property and the derived C_p is also different. In Section III-D, an intuitive eqivalent circuit model of Fig. 1(a) will be given for a more complete comparison with the traditional architecture.

At V_o, the −3-dB passband bandwidth $(2\Delta f_{o3\text{ dB}})$ can be derived next, assuming $R_{sw} = 0$ for simplicity. The gain from V_{RF} to V_o at frequency $f_s - \Delta f_{o3\text{ dB}}$ is given by

$$A_{vo}|_{@f_s - \Delta f_o 3\text{ dB}} = \frac{V_o}{V_{RF}} = \frac{R_L(1 - g_m Z_T)}{2R_S(1 + g_m R_L)} \tag{6}$$

where

$$Z_T = jL_{eff}//R_{F1}//R_p \text{ and } L_{eff} \approx \frac{\omega_s - \Delta\omega_{o3\text{ dB}}}{2\frac{\Delta\omega_{o3\text{ dB}}}{\omega_s}} L_p. \tag{7}$$

From the definition of −3-dB passband bandwidth

$$\frac{\left|A_{vo|_{@f_s}}\right|}{\left|A_{vo|@f_s - \Delta f_o 3\text{ dB}}\right|} = \frac{|1 - g_m R_{FP}|}{|1 - g_m Z_T|} = \sqrt{2} \tag{8}$$

where $A_{vo|_{@f_s}}$ is the voltage gain at the resonant frequency, while $R_{FP} = R_{F1}//R_P$. Substituting (6), (7) into (8), (9) is obtained after simplification

$$L_{eff} = \frac{\sqrt{g_m^2 R_{FP}^2 - 2g_m R_{FP} - 1} \times R_{FP}}{g_m R_{FP} - 1} \approx R_{FP}. \tag{9}$$

Substituting (9) into (7), $\Delta\omega_{o3\text{ dB}}$ becomes

$$\Delta\omega_{o3\text{ dB}} = \frac{\omega_s^2}{2\frac{L_{eff}}{L_p} + \omega_s} \approx \frac{\omega_s^2}{2\frac{L_{eff}}{L_p}} = \frac{1}{2L_{eff}C_p} = \frac{1}{2R_{FP}C_p}. \tag{10}$$

Finally, $2\Delta f_{o3\text{ dB}}$ at V_o can be approximated as

$$2\Delta f_{o3\text{ dB}}|_{@V_o} \approx \frac{1}{\pi R_{FP} C_p}.$$

C. Derivation of the $R_p - L_p - C_p$ Model Using the LPTV Analysis

The GB-BPF [Fig. 1(a)] can be classified as a LPTV system. This section derives the $R_p - L_p - C_p$ model of the gain-boosted N-path SC branch. Similar to [12], [13], the voltage on the SC branch is defined as

$$V_{Ci}(j\omega) = \sum_{n=-\infty}^{\infty} H_{n,RF}(j\omega) V_{RF}\left(j(\omega - n\omega_s)\right). \tag{11}$$

Here n indicates a harmonic number of f_s, and $H_{n,RF}(j\omega)$ is the nth harmonic transfer function associated with the frequency nf_s. With $V_{ci}(j\omega)$, the voltages at $V_i(j\omega)$ and $V_o(j\omega)$ can be related to the input RF signal $V_{RF}(j\omega)$

$$V_i(j\omega) = \underbrace{V_{RF}(j\omega)\frac{1}{\gamma}\left(\beta\frac{R_L}{R_S} + H_{0,RF}(j\omega)\right)}_{V_{i,de}} + \underbrace{\frac{1}{\gamma}\sum_{n=-\infty, n\neq 0}^{\infty} H_{n,RF}(j\omega) V_{RF}\left(j(\omega - n\omega_s)\right)}_{V_{i,un}} \tag{12}$$

and

$$V_o(j\omega) = \underbrace{\frac{R_{F1}R_L\left(1 - g_m R_{sw} + \frac{R_{sw}}{R_{F1}}\right)}{R_{F1}R_{SW} + (R_{F1} + R_{sw})(R_s + g_m R_L R_s + R_L)}}_{V_{o,de}} \times \underbrace{\left[V_{RF}(j\omega) - \frac{H_{0,RF}(j\omega)V_{RF}(j\omega)(1 + g_m R_s)}{\left(1 - g_m R_{sw} + \frac{R_{sw}}{R_{F1}}\right)}\right]}_{V_{o,de}} - \underbrace{\frac{R_{F1}R_L(1+g_m R_s)}{R_{F1}R_{SW}+(R_{F1}+R_{sw})(R_s+g_m R_L R_s+R_L)}}_{V_{o,un}} \times \underbrace{\sum_{n=-\infty, n\neq 0}^{\infty} H_{n,RF}(j\omega) V_{RF}\left(j(\omega - n\omega_s)\right)}_{V_{o,un}}. \tag{13}$$

where

$$\alpha = 1 - g_m R_{sw} + \frac{R_{sw}}{R_{F1}}$$
$$\beta = 1 + \frac{R_{sw}}{R_L} + \frac{R_{sw}}{R_{F1}}$$
$$\gamma = \alpha + \beta\left(\frac{R_L}{R_S} + g_m R_L\right).$$

Equations (12) and (13) can be divided into two parts: 1) the desired frequency selectivity (i.e., $V_{i,de}$ and $V_{o,de}$) that provides

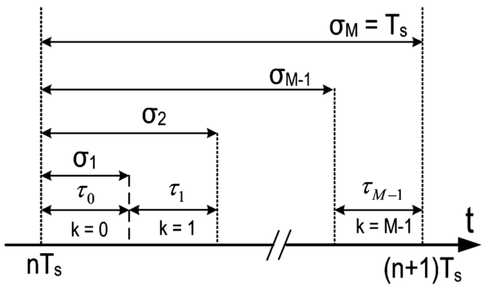

Fig. 4. Time intervals for the state-space analysis.

filtering without frequency translation at the desired input frequency, and 2) the undesired harmonic folding components that might fall in the desired band (i.e., $V_{i,un}$ and $V_{o,un}$).

To find $H_{n,RF}(j\omega)$, a state-space analysis is conducted. The timing diagram for the analysis is shown in Fig. 4. The timing interval $nT_s < t < nT_s + T_s$ is divided into M portions (M is the number of the states) and each portion, identified by k, can be represented as $nT_s+\sigma_k < t < nT_s+\sigma_{k+1}, k = 0, \ldots, M-1$ and $\sigma_0 = 0$. During each interval there is no change in the state of the switches, and the network can be considered as a LTI system. During the k interval, linear analysis applied to Fig. 1(a) reveals that the switch on interval k has the following state-space description:

$$\begin{cases} \frac{C_i dv_{Ci}(t)}{dt} + \frac{v_i(t)-v_o(t)}{R_{F1}} = \frac{v_o(t)}{R_L} + g_m v_i(t) \\ \frac{v_{RF}(t)-v_i(t)}{R_S} = \frac{v_o(t)}{R_L} + g_m v_i(t) \\ v_i(t) = v_{Ci}(t) + v_o(t) + R_{sw}\frac{C_i dv_{Ci}(t)}{dt}. \end{cases} \quad (14)$$

From (14), we obtain

$$\frac{dv_{Ci}(t)}{dt} = \frac{v_{RF}(t)}{C_i R_1} - \frac{v_{Ci}(t)}{C_i R_2} \quad (15)$$

where

$$R_1 = \frac{1 + \frac{R_{sw}}{R_{F1}} + \frac{R_{sw}+R_S}{R_L} + \frac{R_{sw}R_S}{R_{F1}R_L} + g_m R_S + \frac{g_m R_{sw} R_S}{R_{F1}}}{\frac{1}{R_L} + g_m}$$

$$R_2 = \frac{1 + \frac{R_{sw}}{R_{F1}} + \frac{R_{sw}+R_S}{R_L} + \frac{R_{sw}R_S}{R_{F1}R_L} + g_m R_S + \frac{g_m R_{sw} R_S}{R_{F1}}}{\frac{1}{R_{F1}} + \frac{1}{R_L} + \frac{R_S}{R_{F1}R_L} + \frac{g_m R_S}{R_{F1}}}.$$

By applying the state-space analysis for the circuit in Fig. 1(a), the harmonic transfer function can be derived as

$$H_{n,RF}(j\omega) = \sum_{m=0}^{N-1} e^{-jn\omega_s\sigma_m} H_{n,m}(j\omega)$$

$$H_{n,m}(j\omega) = \frac{\omega_{rc,B}}{\omega_{rc,A} + j\omega} \times \frac{1 - e^{-jn\omega_s\tau_m}}{j2\pi n} + \frac{1 - e^{j(\omega-n\omega_s)(T_S-\tau_m)-jn\omega_s\tau_m}}{\omega_{rc,A}+j\omega} G(j\omega) f_s \quad (16)$$

where

$$G(j\omega) = \frac{e^{j(\omega-n\omega_s)\tau_m} - e^{-\omega_{rc,A}\tau_m}}{e^{j2\pi(\omega-n\omega_s)/\omega_s} - e^{-\omega_{rc,A}\tau_m}} \times \frac{1}{\frac{\omega_{rc,A}}{\omega_{rc,B}} + \frac{j(\omega-n\omega_s)}{\omega_{rc,B}}}$$

and where $\omega_{rc,A} = 1/R_2C_i$ and $\omega_{rc,B} = 1/R_1C_i$. The above $H_{n,RF}(j\omega)$ is undefined for $n = 0$, and, for this value, (16) will be defined by the limit when n tends to zero, implying that

$$H_{0,RF}(j\omega) = \frac{\omega_{rc,B}}{\omega_{rc,A} + j\omega} + \frac{1 - e^{j\omega(T_S-\tau_m)}}{\omega_{rc,A} + j\omega} G(j\omega) f_s N \quad (17)$$

where

$$G(j\omega) = \frac{e^{j\omega\tau_m} - e^{\omega_{rc,A}\tau_m}}{e^{\frac{j2\pi\omega}{\omega_s}} - e^{-\omega_{rc,A}\tau_m}} \times \frac{1}{\frac{somega_{rc,A}}{\omega_{rc,B}} + \frac{j\omega}{\omega_{rc,B}}}.$$

To find R_p, $H_{0,RF}(j\omega)$ is calculated at $\omega = nf_s$ with $\omega_s \gg \omega_{rc,A}, \omega_{rc,B}$, yielding

$$H_{0,RF}(jn\omega_s) = \frac{2N(1 - \cos 2\pi nD)}{4D(n\pi)^2} \times \frac{\omega_{rc,B}}{\omega_{rc,A}} \quad (18)$$

where $D = 1/N$ is the duty cycle of the LO. Furthermore, (18) is similar to (15) in [10], except for the added term $\omega_{rc,B}/\omega_{rc,A}$.

If $n = 1$, $N = 4$ and $D = 0.25$, for a 25%-duty-cycle four-path LO, (18) becomes

$$H_{0,RF}(j\omega_s) = \frac{8}{\pi^2} \times \frac{R_2}{R_1}. \quad (19)$$

Assuming that L_p is resonant with C_p at ω_s, it implies

$$\begin{cases} \frac{V_i - H_{0,RF}(j\omega_s)V_{RF} - V_o}{R_{sw}} = \frac{H_{0,RF}(j\omega_s)V_{RF}}{R_p} \\ \frac{V_i - H_{0,RF}(j\omega_s)V_{RF} - V_o}{R_{sw}} + \frac{V_i - V_o}{R_{F1}} = g_m V_i + \frac{V_o}{R_L} \\ \frac{V_{RF} - V_i}{R_s} = g_m V_i + \frac{V_o}{R_L}. \end{cases} \quad (20)$$

Solving (20), it leads to the desired R_P

$$R_p = \frac{\eta H_{0,RF} R_{sw}}{\left(\frac{R_L R_{FL}}{R_s} + \frac{H_{0,RF}}{R_{sw}}\right)\left(1 + \frac{R_L}{R_s} + g_m R_L\right) - \left(H_{0,RF} + \frac{R_L}{R_s}\right)\eta}$$

where

$$R_{FL} = \frac{1}{R_L} + \frac{1}{R_{F1}} + \frac{1}{R_{sw}}$$

$$\eta = \frac{1}{R_{sw}} + \frac{1}{R_{F1}} - g_m + \frac{R_L R_{FL}}{R_s} + g_m R_L R_{FL}.$$

Finally, placing the pole around ω_s in (17), with a value equal to the poles of the transfer function from V_{RF} to V_{Cp} of Fig. 1(b), it will lead to the expressions of C_p and L_p

$$C_p = \frac{\gamma_1 + R_p}{2D\omega_{rc,A}\gamma_1 R_p} \quad (21)$$

$$L_p = \frac{\gamma_1 R_p}{D\omega_{rc,A}(\gamma_1 + R_p) - \left(D^2\omega_{rc,A}^2 - \omega_s^2\right)\gamma_1 R_p C_p} \quad (22)$$

where

$$\alpha_1 = \frac{1}{R_{sw}} + \frac{1}{R_{F1}} - g_m,\ \gamma_1 = -\frac{\alpha_1\beta_1 R_{sw}^2}{\beta_1 - 1 - \alpha_1\beta_1 R_{sw}},$$

$$\beta_1 = \frac{\frac{1}{R_L} + \frac{1}{R_{F1}} + \frac{1}{R_{sw}} + \frac{\alpha_1 R_s}{R_L(1+g_m R_s)}}{\frac{1}{R_L} + g_m}.$$

From (21) and (22), C_p is irrelevant to the LO frequency ω_s, while L_p is tunable with ω_s. Moreover, the term $D\omega_{rc,A}(\gamma_1 + R_P) - (D^2\omega_{rc,A}^2 - \omega_s^2)\gamma_1 R_p C_p$ in the denominator of (22) renders that the $L_p//C_p$ resonant frequency shifts slightly away from the center frequency ω_s. For $\omega_s \gg \omega_{rc,A}$, $L_p \approx R_p/\omega_s^2 C_p$ is obtained and will resonate out with C_p at ω_s. Then, the frequency responses can be plotted using the derived expressions, and compared with the simulated curves of Fig. 5(a) and (b); showing a good fitting around ω_s, and confirming the previous analysis. The small discrepancy arises from the approximation that L_p will resonate out with C_p at ω_s when deriving R_p in (20). This effect is smaller at V_i than at V_o, due to the gain of the GB-BPF.

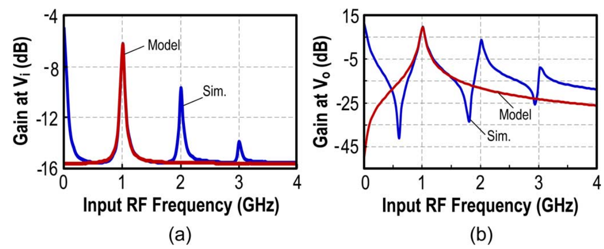

Fig. 5. Comparison between the simulation and the analytic derived model using (21) and (22). (a) Gain at V_i and (b) gain at V_o. The parameters are $R_{sw} = 10\ \Omega$, $R_L = 80\ \Omega$, $R_S = 50\ \Omega$, $C_i = 5$ pF, $g_m = 100$ mS, $R_{F1} = 500\ \Omega$, $f_s = 1$ GHz, and $N = 4$.

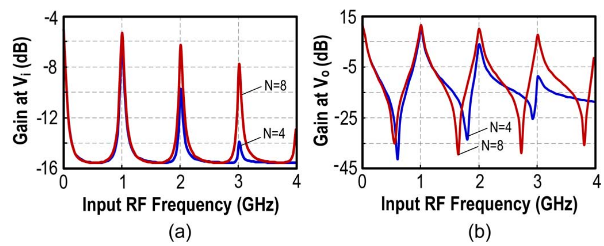

Fig. 6. Simulated responses under $N = 4$ and $N = 8$. (a) Gain at V_i and (b) gain at V_o. The responses are consistent with (17) (not plotted).

III. Harmonic Selectivity, Harmonic Folding, and Noise

A. Harmonic Selectivity and Harmonic Folding

Using the harmonic selectivity function $H_{0,RF}(j\omega)$ from (18), the relative harmonic selectivity is calculated by combining (13) and (18) for V_i and V_o. For example, when $N = 4$

$$\frac{V_0(\omega_s)}{V_0(n\omega_s)} = \frac{1 - \frac{8}{\pi^2} \times \frac{R_2}{R_1} \times \text{Constant}}{1 - \frac{8}{(n\pi)^2} \times \frac{R_2}{R_1} \times \text{Constant}} \approx n^2$$

which matches with the four-path passive mixer [10]. Likewise, using (12) and (18), the harmonic selectivity at V_i is derived as

$$\frac{V_i(\omega_s)}{V_i(n\omega_s)} \approx \frac{R_L + \frac{8}{\pi^2} \times R_{F1}}{R_L + \frac{8}{(n\pi)^2} \times R_{F1}} < n^2.$$

Obviously, the harmonic selectivity at V_i is smaller than that at V_o with the design parameters used here.

The above analysis has ignored the even-order harmonic selectivity which should be considered in single-ended designs. The harmonic selectivity for $N = 4$ and $N = 8$ with a fixed total value of capacitance and $g_m R_{sw} = 1$ are shown in Fig. 6(a) and 6(b), respectively. For $N = 4$, $V_o(3\omega_s)/V_o(\omega_s) = 18.67$ dB and $V_i(3\omega_s)/V_i(\omega_s) = 7.6$ dB, close to the above analysis. Moreover, the relative harmonic selectivity can be decreased by raising N. Furthermore, as derived in (4), $g_m R_{sw} = 1$ results in a stronger OB attenuation at far out frequencies that are irrelevant to N. Finally, the bandwidth at V_i and V_o can be kept constant if the total amount of capacitors is fixed under different N. This will be quite explicit when the equivalent circuit will be presented later in Section III-C.

For $N = 4$, the simulated harmonic folding at V_i and V_o are shown in Fig. 7(a) and (b), respectively, which obey well (12), (13), and (16) (not plotted). Similar to the N-path passive mixers, the input frequencies around $k(N \pm 1)f_s$ will be folded onto the desired frequency around f_s. The strongest folding term is from $3f_s$ when $k = 1$, and will become smaller if k (integer number) is increased. The relative harmonic folding $\Delta HF_i = 20\log[V_{i,de}(j\omega)] - 20\log[V_{i,un}(j\omega)]$ and $\Delta HF_o = 20\log[V_{o,de}(j\omega)] - 20\log[V_{o,un}(j\omega)]$ are plotted in Fig. 8(a) and (b), respectively. The relative harmonic folding is smaller at V_i than at V_o, which is preferable because harmonic folding at V_i cannot be filtered.

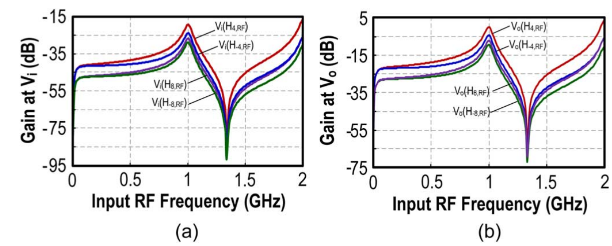

Fig. 7. Simulated harmonic folding effects under $N = 4$. (a) Gain at V_i and (b) gain at V_o. The responses are consistent with (16) (not plotted).

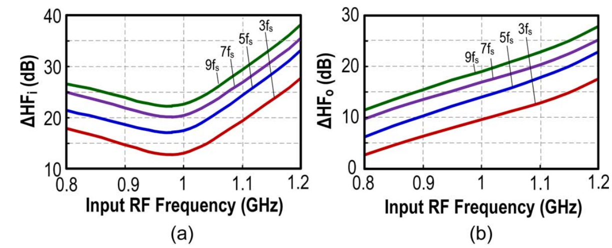

Fig. 8. Simulated harmonic folding gain (normalized) under $N = 4$ (a) at V_i and (b) V_o.

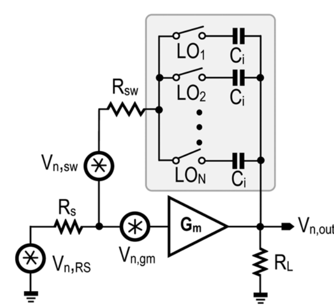

Fig. 9. Equivalent noise model of the GB-BPF.

B. Noise

The output noises under consideration are the thermal noises from R_s, R_{sw} and G_m. Since the power spectral density (PSD) of these noise sources are wideband, harmonic folding noise should be considered. The model to derive those noise transfer functions is shown in Fig. 9.

To calculate the noise from R_s to V_o (13) needs to be revised in order to obtain

$$\overline{V_{n,out,RS}^2} = \underbrace{\left| \frac{R_{F1}R_L\left(1 - g_m R_{sw} + \frac{R_{sw}}{R_{F1}}\right)}{R_{F1}R_{SW} + (R_{F1} + R_{sw})(R_s + g_m R_L R_s + R_L)} \right|^2}_{\text{Part A}} \times \underbrace{|V_{n,RS}(j\omega)|^2 \times \left| 1 - \frac{H_{0,RF}(j\omega)(1 + g_m R_s)}{\left(1 - g_m R_{sw} + \frac{R_{sw}}{R_{F1}}\right)} \right|^2}_{\text{Part A}}$$

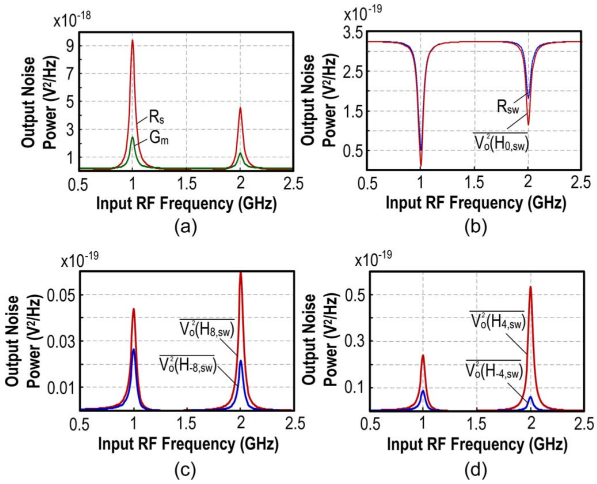

Fig. 10. Simulated output noise power at V_o due to (a) R_S and G_m and (b) R_{sw}. The results are consistent with (23), (25), and (27) (not plotted). The output noise power $\overline{V_o^2(H_0(j\omega))}$ with notch shape of R_{sw} is plotted in (b) using (25) Part A. The harmonic folding parts $\overline{V_o^2(H_{\pm 4}(j\omega))}$ and $\overline{V_o^2(H_{\pm 8}(j\omega))}$ using (25) Part B are plotted in (c) and (d). The parameters are $R_{sw} = 30\ \Omega$, $R_L = 80\ \Omega$, $R_S = 50\ \Omega$, $C_i = 5$ pF, $g_m = 100$ mS, $R_{F1} = 500\ \Omega$, $f_s = 1$ GHz, $N = 4$, $\overline{V_{n,sw}^2} = 4kTR_{sw} = 4.968 \times 10^{-19}$ (V^2/Hz), $\overline{V_{n,Rs}^2} = 4kTR_s = 8.28 \times 10^{-19}$ (V^2/Hz), and $\overline{V_{n,gm}^2} = 4kT/g_m = 1.656 \times 10^{-19}$ (V^2/Hz).

$$+\underbrace{\left|\frac{R_{F1}R_L(1+g_mR_s)}{R_{F1}R_{SW}+(R_{F1}+R_{sw})(R_s+g_mR_LR_s+R_L)}\right|^2}_{\text{Part B}}$$

$$\underbrace{\times \sum_{n=-\infty, n\neq 0}^{\infty} \left|H_{n,RF}(j\omega)V_{n,RS}\left(j(\omega - n\omega_s)\right)\right|^2}_{\text{Part B}}. \quad (23)$$

In (23), Part A is the output noise PSD due to R_s without frequency translation, while Part B is due to harmonic folding. Similarly, linear analysis of $\upsilon_{n,sw}(t)$ results in the state-space description

$$\frac{d\upsilon_{Ci}(t)}{dt} = \frac{\upsilon_{n,sw}(t)}{C_iR_1} - \frac{\upsilon_{Ci}(t)}{C_iR_2} \quad (24)$$

where

$$R_1 = \frac{-(1+\alpha_2R_{sw})}{\alpha_2}$$
$$R_2 = -R_1$$
$$\alpha_2 = \frac{\left(\frac{1}{R_{F1}} + \frac{1}{R_S} + \frac{R_L}{R_{F1}R_S} + \frac{g_mR_L}{R_{F1}}\right)}{\left(1 + g_mR_L + \frac{R_L}{R_S}\right)}$$

with a minus sign in R_1. Combining (24) with (16) and (17), the output noise PSD transfer function of R_{sw} from $V_{n,sw}$ to V_{ci} [i.e., $H_{0,sw}(j\omega)$] and its harmonic folding [i.e., $H_{n,sw}(j\omega)$] can be derived, leading to the final output noise of PSD to V_o expressed as

$$\overline{V_{n,out,sw}^2} = \underbrace{\frac{|V_{n,sw}(j\omega)|^2\,|(1+H_{0,sw})|^2}{\left|\left(-\frac{R_S}{\gamma_2R_L} - 1 - \frac{R_{sw}}{\gamma_2R_L} - \frac{R_{sw}}{R_{F1}} - \frac{R_{sw}R_S}{\gamma_2R_LR_{F1}}\right)\right|^2}}_{\text{Part A}}$$

$$+\underbrace{\sum_{n=-\infty, n\neq 0}^{\infty} \left|\frac{H_{n,sw}(j\omega)V_{n,sw}(j\omega - jn\omega_s)}{-\frac{R_S}{\gamma_2R_L} - 1 - \frac{R_{sw}}{\gamma_2R_L} - \frac{R_{sw}}{R_{F1}} - \frac{R_{sw}R_S}{\gamma_2R_LR_{F1}}}\right|^2}_{\text{Part B}} \quad (25)$$

where

$$\gamma_2 = 1 + g_mR_s.$$

In (25), Part A is the noise transfer function without harmonic folding, while Part B corresponds to the harmonic folding. Similarly, linear analysis of $\upsilon_{n,gm}(t)$ has the state-space description

$$\frac{d\upsilon_{Ci}(t)}{dt} = \frac{\upsilon_{n,gm}(t)}{C_iR_1} - \frac{\upsilon_{Ci}(t)}{C_iR_2} \quad (26)$$

where

$$R_1 = \frac{\alpha_3 + \frac{R_s}{R_L}}{\alpha_3\beta_3 + \beta_3\frac{R_s}{R_L} - \gamma_3g_mR_s},\ R_2 = \frac{\alpha_3 + \frac{R_s}{R_L}}{\alpha_3\gamma_3}$$
$$\alpha_3 = 1 + g_mR_s,\ \beta_3 = \frac{g_m}{\alpha_3}\left(\frac{R_s}{R_{F1}} + 1\right)$$
$$\gamma_3 = \frac{1}{R_L} + \frac{1}{R_{F1}} - \frac{g_mR_s}{\alpha_3R_L} + \frac{R_s}{\alpha_3R_LR_{F1}}.$$

From (26) together with (16) and (17), the output noise PSD transfer function of G_m stage from $V_{n,gm}$ to V_{ci} [i.e., $H_{0,gm}(j\omega)$] and its harmonic folding [i.e., $H_{n,gm}(j\omega)$] can be derived. Finally, the output noise PSD to V_o is

$$\overline{V_{n,out,gm}^2} = \underbrace{\frac{|V_{n,gm}(j\omega)|^2\left|g_m + H_{0,gm}g_m + \frac{H_{0,gm}}{R_S}\right|^2}{\left|\frac{1}{R_s} + \frac{1}{R_L} + g_m\right|^2}}_{\text{Part A}}$$

$$+\underbrace{\sum_{n=-\infty, n\neq 0}^{\infty} \left|g_m\frac{H_{n,gm}(j\omega)V_{n,gm}(j\omega - jn\omega_s)}{\frac{1}{R_s} + \frac{1}{R_L} + g_m}\right|^2}_{\text{Part B}}. \quad (27)$$

The simulated output noises at V_o due to $\upsilon_{n,RS}(t)$ and $\upsilon_{n,gm}(t)$ are shown in Fig. 10(a), whereas Fig. 10(b) and (c) show the output noise due to $\upsilon_{n,sw}(t)$ and its key harmonic folding terms, respectively. Similar to the signal transfer function, the output noises from R_S and G_m are alike a comb, and can be considered as narrowband around $n\omega_s$. Unlike the traditional wideband LNAs that have wideband output noise, here the output noise around the LO harmonics is much less than that at the LO first harmonic. Thus, a wideband passive mixer follows the GB-BPF for downconversion, with the noise due to harmonic folding being much relaxed. Besides, the noise transfer function of R_{sw} is a notch function, while its harmonic folding terms are bandpass with much smaller amplitude. This is also true for the conventional N-path passive mixer as analyzed in [16, eq. 45] with a difference method. Around $n\omega_s$ where the in-band signal exists, the main contribution to its noise is the folding from higher harmonics, which is much less than the OB noise. The noise from R_{sw} is thus greatly suppressed, and a larger R_{sw} is allowed to relax the LO power. In other words, by re-sizing g_m, smaller switches can be used for the SC branch while keeping a high OB selectivity filtering profile as analyzed in Section II.

C. Intuitive Equivalent Circuit Model

As shown in Fig. 5(a) and (b), the filtering behavior at both V_i and V_o are similar to that of a single-ended passive mixer, which motivates the remodeling of the circuit in Fig. 1(a) with two sets of single-ended passive mixers: one at V_i and one at V_o, as shown in Fig. 11(a). With the proposed intuitive equivalent circuit, it is convenient to include the parasitic capacitances at

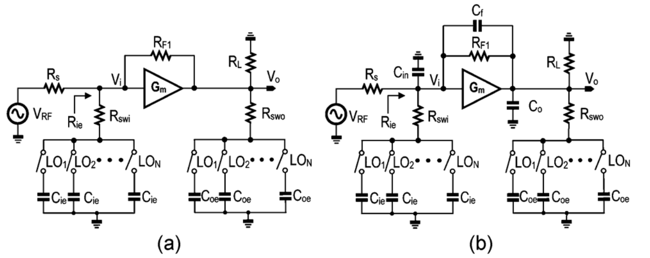

Fig. 11. Intuitive equivalent circuit of the GB-BPF. (a) Typical G_m and (b) a non-ideal G_m with parasitic capacitances C_{in}, C_o, and C_f.

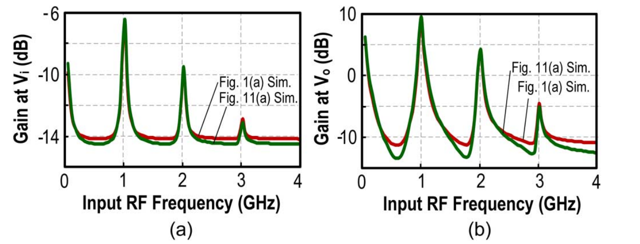

Fig. 12. Simulation comparison of Figs. 1(a) and 11(a). (a) Gain at V_i and (b) gain at V_o. The parameters are $R_{sw} = 30\ \Omega$, $R_L = 80\ \Omega$, $R_S = 50\ \Omega$, $C_i = 5$ pF, $g_m = 100$ mS, $R_{F1} = 500\ \Omega$, $f_{Lo} = 1$ GHz, and $N = 4$.

both V_i and V_o by using a known theory developed in [14], [15] as shown in Fig. 11(b). The non-idealities due to LO phase/duty cycle mismatch can be analyzed similar to [14], while the variation of g_m to the in-band gain is similar to the condition of a simple inverter since the two sets of passive mixer are of high impedance at the clock frequency. Inside, we remodel the switch's on-resistance as R_{swi} at V_i with capacitance C_{ie}, and R_{swo} at V_o with capacitance C_{oe}.

$$\begin{cases} R_{swi} = \frac{(R_{sw}//R_{F1})+R_L}{1+g_mR_L} \approx \frac{R_{sw}+R_L}{1+g_mR_L} \\ C_{ie} = \left|\frac{(1-g_mR_{F1})R_L}{R_L+R_{F1}}\right| \times C_i \\ R_{swo} = \frac{(R_{sw}//R_{F1})+R_s}{1+g_mR_s} \\ C_{oe} = C_i. \end{cases} \tag{28}$$

R_{swi} described in (28) equals to (2). Thus, for far-out blockers, $R_{swi}//R_{ie}$ is smaller than R_i, which results in better ultimate rejection [Fig. 11(a)]. The value of C_{ie} is obvious, it equals the gain of the circuit multiplied by C_i, but without the SC branch in the feedback. It can be designated as the open-SC gain, and it can be enlarged to save area for a specific -3-dB bandwidth. As an example, with $R_L = 80\ \Omega$, $R_{sw} = 30\ \Omega$, $R_S = 50\ \Omega$, $C_i = 5$ pF, $g_m = 100$ mS and $R_{F1} = 500\ \Omega$, C_{ie} is calculated to be 33.79 pF, which is $\sim 6\times$ smaller than C_i in the traditional design [10], thus the area saving in C_i is significant. For R_{swo}, it equals the output resistance with R_{sw} in the feedback. This is an approximated model without considering the loading from R_{swi} to R_{swo}.

To verify it, the frequency responses of Fig. 1(a) and Fig. 11(a) are plotted together in Fig. 12(a) and (b) for comparison. It is observed that their -3-dB bandwidth and gain around ω_s fit well with each other, since the loading from the mutual coupling between the SC for IB signal is less an issue than that of OB blockers. As expected, the ultimate rejection in Fig. 11(a) is better than that in Fig. 1(a). Note that the parasitic capacitances C_{in} at V_i and C_o at V_o have been included in Fig. 11(b). Also, to account C_{gs} of the G_m's two MOSFETs [Fig. 1(a)], a parasitic capacitance C_f is placed in parallel with R_{F1}. Still, the accuracy of the equivalent circuit is acceptable around f_s, as shown in Fig. 13(a) and (b). It is noteworthy that the gain at around ω_s fits better with each other than that of $2\omega_s$, $3\omega_s$, etc. For the influence of C_{in} and C_o, it mainly lowers the IB gain and slightly shifts the resonant frequency [4], [14]. For C_f, it induces Miller equivalent capacitances at V_i and V_o, further lowering the gain and shifting the center frequency. With (28) and the RLC model, the -3-dB bandwidth at V_i is derived as

$$2\Delta f_{i3\text{ dB}} = \frac{1}{4\pi\left(R_s//\frac{R_{F1}+R_L}{1+g_mR_L}\right)C_{ie}}.$$

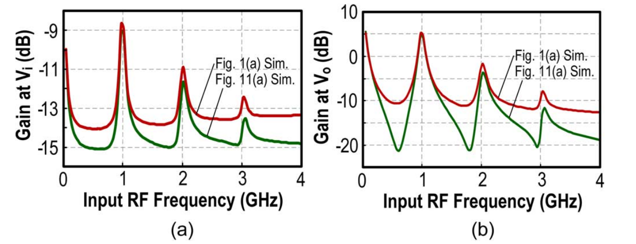

Fig. 13. Simulation comparison of Figs. 1(a) and 11(b). (a) Gain at V_i and (b) gain at V_o. The parameters are the same as Fig. 12, with the additional $C_{in} = 1$ pF, $C_o = 1$ pF, and $C_f = 500$ fF.

TABLE I
KEY PARAMETERS IN THE DESIGN EXAMPLE

g_m (mS)	R_{sw} (Ω)	R_{F1} (Ω)	R_L (Ω)	C_i (pF)
76	20	1k	120	5

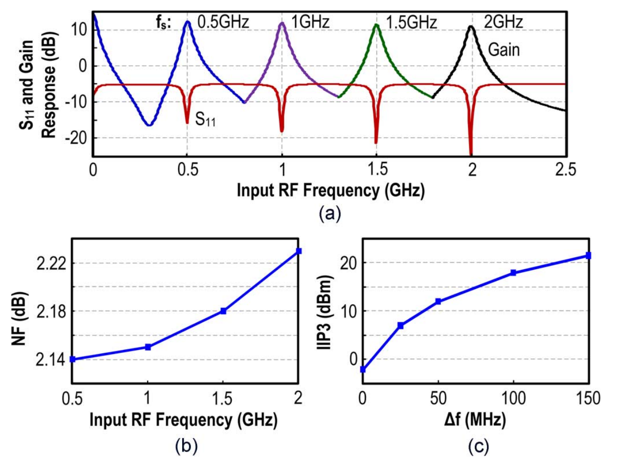

Fig. 14. Simulated (a) voltage gain and S_{11} with different f_s showing the LO-defined bandpass responses. (b) NF versus input RF frequency. (c) IB and OB IIP3.

IV. Design Example

A four-path GB-BPF suitable for full-band mobile-TV or IEEE 802.11af cognitive radio is designed and simulated with 65-nm GP CMOS technology. The circuit parameters are summarized in Table I. The transistor sizes for the self-biased inverter-based G_m are: $(W/L)_{PMOS} = (24/0.1) \times 4$ and $(W/L)_{NMOS} = (12/0.1) \times 4$. The 0.1-$\mu$m channel length is to raise the gain for a given power and g_m value. The switches are NMOS with $(W/L)_{sw} = 25/0.06$. C_i is realized with MiM capacitor.

TABLE II
SIMULATED PERFORMANCE SUMMARY IN 65-nm CMOS

Tunable RF (GHz)	0.5 to 2
Gain (dB)	11 to 12.5
NF (dB)	2.14 to 2.23
$IIP3_{IB}$ (dBm)*	-2
$IIP3_{OB}$ (dBm) (Δf = +25 MHz)*	+7
$IIP3_{OB}$ (dBm) (Δf = +50 MHz)*	+12
$IIP3_{OB}$ (dBm) (Δf = +100 MHz)*	+18
$IIP3_{OB}$ (dBm) (Δf = +150 MHz)*	+21.5
BW (MHz)	41 to 48
Power (mW) @ Supply (V)	7 @ 1

$^{*}f_s = 500$ MHz, two tones at $f_s + \Delta f + 2$ MHz and $f_s + 2\Delta f + 4$ MHz.

As shown in Fig. 14(a), the passband is LO-defined under $f_s = 0.5$, 1, 1.5, and 2 GHz and $S_{11} < -15$ dB in all cases. The -3-dB BW ranges between 41 to 48 MHz, and is achieved with a total MiM capacitance of 20 pF. The calculated C_{ie} based on (28) is thus $\sim$40 pF, and the required C_{ie} for four paths is 160 pF. The -3-dB BW at 2 GHz is larger due the parasitic capacitor that reduces the Q of the GB-BPF. The gain is 12.5 dB at 0.5-GHz RF, which drops to 11 dB at 2-GHz RF with an increase of NF by $<$0.1 dB as shown in Fig. 14(b). The IIP3 improves from IB (-2 dBm) to OB ($+21.5$ dBm at 150-MHz offset) as shown in Fig. 14(c). For the circuit non-idealities, 10% of LO duty cycle mismatch only induce a small variation of IB gain by around 0.05 dB. For a g_m variation of 10%, the IB gain variation is 0.07 dB at 500-MHz LO frequency. The performance summary is given in Table II.

V. CONCLUSIONS

This paper has described the analysis, modeling and design of a GB-BPF that features a number of attractive properties. By using a transconductance amplifier (G_m) as the forward path and an N-path SC branch as its feedback path, double RF filtering at the input and output ports of the G_m is achieved concurrently. Moreover, when designed for input impedance matching, both in-band gain and bandwidth can be customized due to the flexibility created by G_m. Both the power and area efficiencies are improved when compared with the traditional passive N-path filter due the loop gain offered by G_m. All gain and bandwidth characteristics have been verified using a RLC model first, and later with the LPTV analysis to derive the R, L, and C expressions. The harmonic selectivity, harmonic folding and noise have been analyzed and verified by simulations, revealing that the noise of the switches is notched at the output, benefitting the use of small switches for the SC branch, saving the LO power without sacrificing the selectivity. The design example is a four-path GB-BPF. It shows $>$11 dB gain, $<$2.3-dB NF over 0.5–2-GHz RF, and $+$21-dBm out-of-band IIP3 at 150-MHz offset, at just 7 mW of power. The developed models also backup the design of the ultra-low-power receiver in [9] for multiband sub-GHz ZigBee applications.

REFERENCES

[1] C. Andrews and A. Molnar, "A passive mixer-first receiver with digitally controlled and widely tunable RF interface," *IEEE J. Solid-State Circuits*, vol. 45, no. 12, pp. 2696–2708, Dec. 2010.

[2] C. Andrews and A. Molnar, "Implications of passive mixer transparency for impedance matching and noise figure in passive mixer-first receivers," *IEEE Trans. Circuits Syst. I, Reg. Papers*, vol. 57, no. 12, pp. 3092–3103, Dec. 2010.

[3] D. Murphy, H. Darabi, A. Abidi, A. Hafez, A. Mirzaei, M. Mikhemar, and M. Chang, "A blocker-tolerant, noise-cancelling receiver suitable for wideband wireless applications," *IEEE J. Solid-State Circuits*, vol. 47, no. 12, pp. 2943–2963, Dec. 2012.

[4] M. Darvishi, R. van der Zee, and B. Nauta, "Design of active N-path filters," *IEEE J. Solid-State Circuits*, vol. 48, no. 12, pp. 2962–2976, Dec. 2013.

[5] A. Mirzaei, H. Darabi, A. Yazdi, Z. Zhou, E. Chang, and P. Suri, " A 65 nm CMOS quad-band SAW-less receiver SOC for GSM/GPRS/EDGE," *IEEE J. Solid-State Circuits*, vol. 46, no. 4, pp. 950–964, Apr. 2011.

[6] A. Mirzaei, H. Darabi, and D. Murphy, "A low-power process-scalable superheterodyne receiver with integrated high-Q filters," in *ISSCC Dig. Tech. Papers*, Feb. 2011, pp. 60–61.

[7] S. Youssef, R. van der Zee, and B. Nauta, "Active feedback technique for RF channel selection in front-end receivers," *IEEE J. Solid-State Circuits*, vol. 47, no. 12, pp. 3130–3144, Dec. 2012.

[8] M. Darvishi, R. van der Zee, E. Klumperink, and B. Nauta, "Widely tunable 4th order switched G_m-C band-pass filter based on N-path filters," *IEEE J. Solid-State Circuits*, vol. 47, no. 12, pp. 3105–3119, Dec. 2012.

[9] Z. Lin, P.-I. Mak, and R. P. Martins, "A 0.5 V 1.15 mW 0.2 mm^2 sub-GHz ZigBee receiver supporting 433/860/915/960 MHz ISM bands with zero external components," in *ISSCC Dig. Tech. Papers*, Feb. 2014, pp. 164–165.

[10] A. Ghaffari, E. Klumperink, M. Soer, and B. Nauta, "Tunable high-Q N-path band-pass filters: Modeling and verification," *IEEE J. Solid State Circuits*, vol. 46, no. 5, pp. 998–1010, May 2011.

[11] B. Razavi, *RF Microelectronics*, 2nd ed. Englewood Cliffs, NJ, USA: Prentice-Hall, 2011.

[12] M. Soer, E. Klumperink, P. deBoer, F. vanVliet, and B. Nauta, "Unified frequency domain analysis of switched-series-RC passive mixers and samplers," *IEEE Trans. Circuits Syst. I, Reg. Papers*, vol. 57, no. 10, pp. 2618–2631, Oct. 2010.

[13] A. Ghaffari, E. Klumperink, M. Soer, and B. Nauta, "Tunable N-path Notch filters for blocker suppression: Modeling and verification," *IEEE J. Solid-State Circuits*, vol. 48, no. 6, pp. 1370–1382, Jun. 2013.

[14] A. Mirzaei and H. Darabi, "Analysis of imperfections on performance of 4-phase passive-mixer-based high-Q bandpass filters in SAW-less receivers," *IEEE Trans. Circuits Syst. I, Reg. Papers*, vol. 58, no. 5, pp. 879–892, May 2011.

[15] A. Mirzaei, H. Darabi, and J. Leete *et al.*, "Analysis and optimization of direct-conversion receivers with 25% duty-cycle current-driven passive mixers," *IEEE Trans. Circuits Syst. I, Reg. Papers*, vol. 57, no. 9, pp. 2353–2366, Sep. 2010.

[16] A. Mirzaei, H. Darabi, and H. D. Murphy, "Architectural evolution of integrated M-phase high-Q bandpass filters," *IEEE Trans. Circuits Syst. I, Reg. Papers*, vol. 59, no. 1, pp. 52–65, Jan. 2012.

Zhicheng Lin (S'12) is currently working toward the Ph.D. degree at the State-Key Laboratory of Analog and Mixed-Signal VLSI and FST-ECE, University of Macau, Macau, China. His research interests are on ultra-low-power radios and multiband multistandard wireless receivers in CMOS.

Pui-In Mak (S'00–M'08–SM'11) received the Ph.D. degree from the University of Macau (UM), Macao, China, in 2006.

He is currently an Associate Professor at UM, and Coordinator of the Wireless and Biomedical Research Lines of the State-Key Laboratory of Analog and Mixed-Signal VLSI. His research interests are on analog and RF circuits and systems for wireless, biomedical, and physical chemistry applications. His group reported six state-of-the-art chips at ISSCC: wideband receivers (2011, 2014), micropower amplifiers (2012, 2014), and ultra-low-power ZigBee receivers (2013, 2014), and pioneered the world's first Intelligent Digital Microfludic Technology (iDMF) with Nuclear Magnetic Resonance (NMR) and Polymerase Chain Reaction (PCR) capabilties. He has authored two books *Analog-Baseband Architectures and Circuits for Multistandard and Low-Voltage Wireless Transceivers* (Springer, 2007), and *High-/Mixed-Voltage Analog and RF Circuit Techniques for Nanoscale CMOS* (Springer, 2012).

Dr. Mak is an IEEE Distinguished Lecturer and has been a member of Board-of-Governors (2009–2011) of the IEEE Circuits and Systems Society (CASS). He was an Editorial Board Member of the IEEE Press (2014–2016), Senior Editor of the IEEE JOURNAL ON EMERGING AND SELECTED TOPICS IN CIRCUITS AND SYSTEMS (2014–2015), Associate Editor of the IEEE TRANSACTIONS ON CIRCUITS AND SYSTEMS, PART I (TCAS-I) (2010–2011, 2014–present), Associate Editor of the IEEE TRANSACTIONS ON CIRCUITS AND SYSTEMS, PART II (TCAS-II) (2010–2013), and Guest Editor of the IEEE RFIC VIRTUAL JOURNAL (2014) for the issue of LNA. He is a Technical Program Committee member of A-SSCC. He received the IEEE DAC/ISSCC Student Paper Award (2005), the IEEE CASS Outstanding Young Author Award (2010), National Scientific and Technological Progress Award (2011), and Best Associate Editor for TCAS-II (2012–2013). In 2005, he was decorated with the Honorary Title of Value for scientific merits by the Macau Government.

Rui P. Martins (M'88–SM'99–F'08), born on April 30, 1957. He received the Bachelor (five-years), the Masters, and the Ph.D. degrees, as well as the Habilitation for Full Professor in electrical engineering and computers from the Instituto Superior Técnico (IST), TU of Lisbon, Portugal, in 1980, 1985, 1992, and 2001, respectively.

He has been with the Department of Electrical and Computer Engineering (DECE)/IST, TU of Lisbon, since October 1980. Since 1992, he has been on leave from IST, TU of Lisbon, and is also with the Department of Electrical and Computer Engineering, Faculty of Science and Technology (FST), University of Macau (UM), Macao, China, where he has been a Full Professor since 1998. In FST he was the Dean of the Faculty from 1994 to 1997 and he has been Vice-Rector of the University of Macau since 1997. From September 2008, after the reform of the UM Charter, he was nominated after open international recruitment as Vice-Rector (Research) until August 31, 2013. Within the scope of his teaching and research activities he has taught 21 bachelor and master courses and has supervised (or cosupervised) 26 theses, Ph.D. (11), and Masters (15). He has published 12 books, coauthoring (five) and coediting (seven), plus five book chapters; 266 refereed papers, in scientific journals (60) and in conference proceedings (206); as well as other 70 academic works, in a total of 348 publications. He has also coauthored seven U.S. Patents. He has created the Analog and Mixed-Signal VLSI Research Laboratory of UM, elevated in January 2011 to the State Key Laboratory of China (the 1st in Engineering in Macao), being its Founding Director. He is an IEEE Fellow, was the Founding Chairman of the IEEE Macau Section from 2003 to 2005, and of the IEEE Macau Joint-Chapter on Circuits And Systems (CAS)/Communications (COM) from 2005 to 2008 [2009 World Chapter of the Year of the IEEE Circuits and Systems Society (CASS)]. He was the General Chair of the 2008 IEEE Asia-Pacific Conference on Circuits And Systems (APCCAS2008), and was the Vice-President for the Region 10 (Asia, Australia, the Pacific) of IEEE CASS, for the period of 2009 to 2011. He is now the Vice-President (World) Regional Activities and Membership also of the IEEE CASS for the period 2012 to 2013. He was an Associate Editor of the IEEE TRANSACTIONS ON CIRCUITS AND SYSTEMS II: EXPRESS BRIEFS from 2010–2013. He is also a member of the IEEE CASS Fellow Evaluation Committee (Class of 2013). He was the recipient of two government decorations: the Medal of Professional Merit from Macao Government (Portuguese Administration) in 1999 and the Honorary Title of Value from Macao SAR Government (Chinese Administration) in 2001. In July 2010 was elected, unanimously, as Corresponding Member of the Portuguese Academy of Sciences (in Lisbon), being the only Portuguese Academician living in Asia.